

Contents

1	Introduction	1
2	Background	2
2.1	Ion-solid interactions	2
2.2	Simulation of ion-solid interaction	11
3	Experimental Methods	17
3.1	Nanowire synthesis	17
3.2	Modification	19
3.3	Characterization	21
4	Summary and Outlook	27

1 Introduction

2 Background

This chapter will provide a general scientific context for this dissertation. First, a general outline of energetic ion-solid interaction is given. Next, the effects of the interaction between the ion and the electrons in the solid are discussed separately from the collisions of the ion with nuclei in the solid. With this background, the possibilities of simulating ion-solid interactions are discussed, emphasizing effects and literature relevant to the experiments on ion-nanostructure interactions investigated in this thesis.

2.1 Ion-solid interactions

Electronic Energy loss

An energetic ion impinging on a solid will lose its kinetic energy E to the solid over the distance traveled x in a variety of processes. The stopping power S_e is well described for a large energy range by the Bethe (sometimes “Bethe-Bloch”) formula [Bet30, Blo33] derived using the Born approximation perturbation theory on the impact between the ‘fast’ ion and the ‘slow’ electrons in the solid:

$$S = \frac{dE}{dx} = -A \cdot \frac{\rho Z_2 \cdot Z_1^2}{\beta^2} \cdot \left[\ln \left(\frac{B \cdot \beta^2}{Z_2 \cdot (1 - \beta^2)} \right) - \beta^2 \right], \quad (2.1)$$

with A and B positive combinations of constants, ρ the density and Z_2 the atomic number of the target, Z_1 and $\beta = v/c$ the atomic number and relativistic velocity of the ion. Corrections to this formula are es-

2.1 Ion-solid interactions

pecially necessary for low ion energies, but in detail they are dependent on the target composition, the ion energy and ion mass in a non-trivial way. Figure 2.1 illustrates stopping regimes and where corrections are required to the Bethe formula. The figure and discussion are adapted from reference [Sig04].

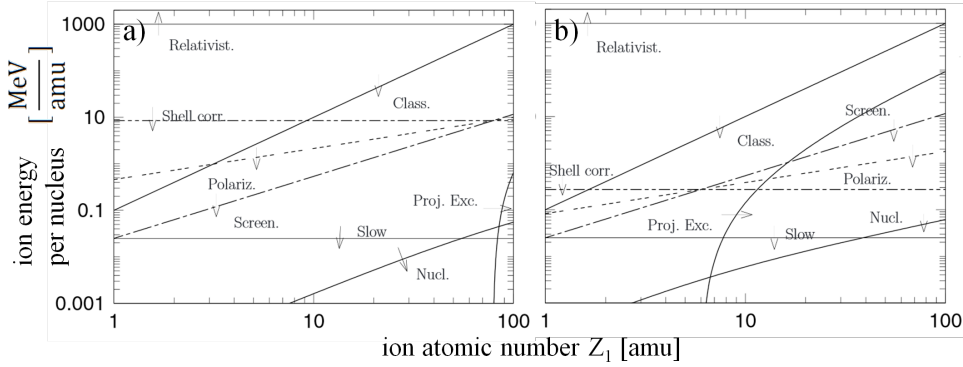


Figure 2.1: Illustration of the dominant effects on the electronic stopping power for an ion of mass Z_1 and energy E in *Au* a) and *C* b). Adapted from [Sig04].

At high ion energies ($> 1 \text{ GeV}/\text{amu}$, labeled “Relativist.”) highly relativistic effects have to be taken into account. At these energies we have, for example, the generation of Cherenkov radiation. The horizontal line labeled “Shell corr.” marks the Thomas-Fermi velocity ($Z_2^{2/3} v_0$) of the target electrons, with the Bohr velocity $v_0 = e^2/\hbar = 25 \text{ keV}/\text{amu}$. In the parameter-space below this line the ion is moving at speeds comparable to that of electrons in the target, so that a correction for the energy levels (shells) in the target has to be made. In the low energy area below the second horizontal line labeled “Slow” (at $25 \text{ keV}/\text{amu}$) the ion is traveling at speeds below the Bohr velocity of the target electrons. Here, the ion velocity is only comparable to that of the valence electrons in the solid. Now the actual electron density distribution and chemical nature of the solid becomes relevant, which is of course not considered in the general Bethe formula. Therefore, for low ion energies a general and accurate theoretical prediction of the stopping power becomes impossible. Specific ion-target combinations require dedicated investigations.

2 Background

Above the line showing the Thomas-Fermi velocity of the ion ($v = Z_1^{2/3}v_0$, “Screen.”) the ion can be assumed to be stripped of all its electrons. Below, an additional screening function must consider the effective charge of the ion, the theoretical framework for the correction is found in the Lindhard theory [Lin54]. Below the curve labeled “Proj. Ext.” the ion (projectile) carries a comparable number of electrons to the target making excitation processes in the electronic configuration of the ion significant.

For ion velocities $v < (Z_1 Z_2)^{1/3}v_0$ (labeled “Polariz.”) a higher order (Z_1^3) correction term to the Bethe formula becomes relevant due to the Barkas-Andersen effect. Barkas et al. found that the stopping power was unequal for particles and anti-particles [SBB53]. This leads to a charge dependent correction term quantified by Andersen et al. [ASS69, SS14]. Below the line marked “Class.” ($Z_1^2 \cdot 100 \text{ keV}/amu$) classical Bohr orbits can be used for electrons around the ion, this is a *sufficient* criterion for the derivation of the Bethe formula not a *necessary* one.

Thus, electronic stopping S_e is the sum of the interactions between the ion and the electrons in the irradiated solid. In the simplest case a target atom is ionized, followed by a host of effects such as characteristic X-ray emission and Auger electron emission associated with the relaxation of this excited state. Analogously, excitation in a semiconductor is associated with band to band transitions, exciton recombination etc. [Wie88, ?]. The luminescent and fluorescent relaxation mechanisms are, however, generally not very efficient. Most of the energy deposited in the electronic system will be turned into kinetic energy of electrons and subsequently converted to phonons/heat. This happens very locally on the nm scale of the electrons mean free path and thus also very quickly, within the order of ps [TDP92, Nas08].

The effects of such local heating on a solid are diverse. Defects and amorphous regions may either appear or disappear, depending on the material and its history. For large ion masses and energies (swift, heavy ions), the deposited energy density becomes large enough to form an “ion track” around the path of the ion. Swift heavy ion tracks are a whole field

2.1 Ion-solid interactions

of research outlined well by references [TDP92, MK97, WKW04]. Very large electronic losses have to be treated carefully as a large percentage of the electrons within the track are energized and some electrons also gain a significant amount of kinetic energy.

The energies used in this dissertation are in the order of $\approx 100\text{ keV}$ with elements of mass $\approx 100\text{ amu}$. The energy regime investigated in this dissertation is thus right at the bottom of the area plotted in figure 2.1. Electronic stopping is not dominant, so that it is sufficient to treat the electronic energy loss as a local heat source.

Nuclear energy loss

In the region marked “Nucl.” in figure 2.1, at low ion energies and for heavy ions, the interaction with the electronic system becomes weak. Here, the contribution of the coulomb interaction between ion and individual target atoms as a whole become the main contribution to slowing down the ion. This is called nuclear stopping in contrast to the electronic stopping discussed in the previous section, as kinetic energy is transferred to the target nuclei, not just the electrons. Its first observation was in the famous Rutherford (Geiger–Marsden) experiment [Rut11] which was groundbreaking to the understanding of the structure of matter. Nuclear energy loss arises from the kinetic energy which is transferred from the energetic ion onto an atom in the target. As the impinging ion can transfer considerable energy to an atom, the atom can leave its lattice site and in turn collide with other atoms in the target, leading to the formation of a collision cascade. This displacement of atoms from their lattice position is the main contribution to irradiation damage and sputtering of the target.

The amorphization of crystalline semiconductors has been investigated extensively, a good review is given by reference [WWS12]. The damage production depends strongly on the properties of the irradiated semiconductor and on the density of the collision cascade caused by the irradiating ion. In general, the defects produced by nuclear energy loss

2 Background

are Frenkel pairs. On further irradiation, interstitials and/or vacancies can agglomerate to form extended defect clusters which initiate amorphization. The ion fluence at which the material is amorphized is highly temperature dependent as Frenkel pairs can anneal at elevated implantation temperatures. This can lead to an arbitrarily high amorphization fluence, if the annealing of defects is faster than their creation. A typical ‘radiation hard’ material is ZnO , which is not amorphous even after 10^{17} cm^{-2} of $200 \text{ keV } Ar^+$ irradiation at 15 K [WWS12]. An arbitrarily large amorphization threshold can also be obtained for Si irradiated with $300 \text{ keV } Ar^+$ at 300° C ($\approx 600 \text{ K}$) [PMB04].

In addition to the activation of defect recombination by increasing the ‘global’ temperature, an increased local temperature by the energy deposited by the ion will also lead to ‘dynamic annealing’ [Dha07]. The reduction of structure sizes leads to larger dynamic annealing as there is less material into which the energy deposited by the ion can dissipate, leading to higher local temperatures. This was shown in the Mn irradiation of $GaAs$ nanowires [Bor12, JHMR15] and was used to improve the magnetic properties of the $GaAs:Mn$ nanowires [BMB⁺11, PKB⁺12, KPJ⁺13, PKJ⁺14].

The binary collision approximation

A typical assumption in the theoretical treatment of nuclear energy loss is the binary collision approximation (BCA) for the ion and the target atoms [Eck91]. Under this assumption nuclear stopping is treated as a series of collisions between single particles. With the additional assumptions of 1) a spherically symmetric interaction potential and 2) the neglect of possible electronic effects (chemical binding) between the collision partners, the angular-momentum is conserved in the collision and the classical scattering-integrals can be solved [ZLB85].

As an example, the resulting trajectories of a $Si-Si$ collision at 10 eV is plotted in figure 2.2. The large difference between the Molière screened Coulomb potential [Mol47] and the “ $Si-Si$ ” potential [HFH⁺90], derived

2.1 Ion-solid interactions

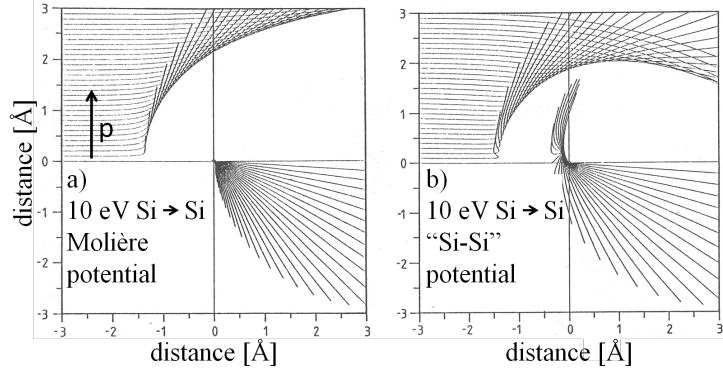


Figure 2.2: Trajectories of a 10 eV *Si-Si* collision for a) Molière and b) “*Si-Si*” potential. The trajectories end after the same elapsed time for each impact parameter p . Adapted from [Eck91].

by Dirac-Fock-Slater calculations, is clearly visible. The former is a purely repulsive Coulomb interaction, while the latter includes an attractive interaction for large interatomic distances similar to the well known Lennard-Jones potential [Jon24, Eck91]. For high energy collisions a “universal” Ziegler-Biersack-Littmark (ZBL) potential based on a screened Coulomb interaction is quite successful [ZLB85], however for low energy collisions a generalized formula cannot be accurate and specific potentials have to be developed for each combination of collision partners [Ded95, NRS97, ANNK02, ND08].

In addition to this problem of finding the correct interaction potential for a collision, depending on the ion and the atomic structure of the irradiated material, the collision parameters relevant to low energy collisions are within the order of the inter-atomic distance of a few Å, as shown in figure 2.2. The assumption that this is still a binary collisions can no longer be valid. In conclusion, it has to be noted that similar to the electronic stopping case, the assumptions for a generalized treatment of nuclear stopping are well fulfilled for large ion energies, but lose their validity at low energies $\ll 1 \text{ keV}$.

2 Background

Sigmund theory of sputtering

A prominent role in this dissertation will be played by a special effect of nuclear energy loss arising when the path of a recoiled atom intersects the targets surface: sputtering. The foundation of a sputter theory was laid by Sigmund [Sig69]. The nuclear stopping of ions leads to the formation of highly branched collision cascades and most of the recoiled atoms are found at the end of the many branches. Because of this, the majority of sputtered particles has a low energy and thus a low range in the material [Tho68]. Therefore, predominantly atoms close to the surface of the target contribute to the sputter yield. The number of atoms sputtered per impinging ion can be estimated by calculating the nuclear energy loss at the surface of the irradiated material, divided by a factor to account for the probability of an atom leaving the solid. The probability for the atom to leave the solid includes geometric considerations and the ‘surface binding energy’ (SBE). A possible model for an atom leaving a solid is that of a potential plateau with the height of the enthalpy of sublimation, which has to be overcome by the atom approaching the surface. This equates the energy required for sputtering an atom to the thermal energy required for sublimation. For metals this is a good assumption, as the metallic bond is undirected and mediated by the electron gas. However, the SBE model for sputtering neglects all effects related to the directionality of the local binding forces experienced by the atom to be sputtered and the modification of the surface by repeated removal of atoms, which will be relevant in compounds with covalent or ionic bonds.

A reasonable assumption for the mean nuclear energy deposition distribution is a Gaussian ellipsoid, with the center at the ion range and the longitudinal and lateral straggling naturally defining its extensions. This approach was used by Sigmund to arrive at a good explanation for the energy dependence of sputtering from flat surfaces [Sig69]. Starting at low ion energies, the sputter yield will initially increase with increasing energy, simply due to more energy being available. For further increasing

2.1 Ion-solid interactions

ion energy, however, the ion range becomes larger, leading to a predominant deposition of the energy deeper inside the target, away from the surface. A maximum is thus found at ion energies where the ion range is in the order of the longitudinal straggling. The angle dependence of sputtering can also be explained by the increased deposition of energy near the surface for larger angles of incidence, as shown in figure 2.3.

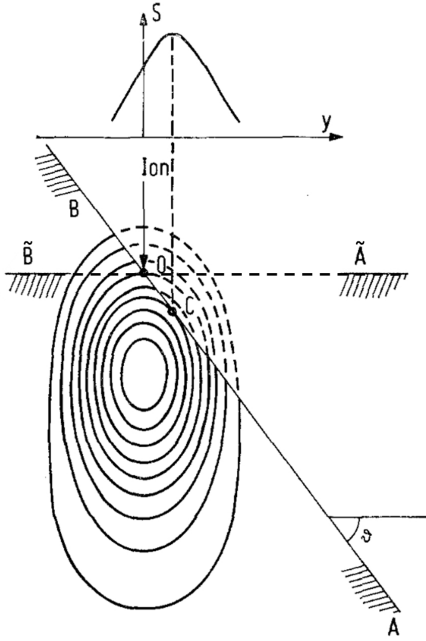


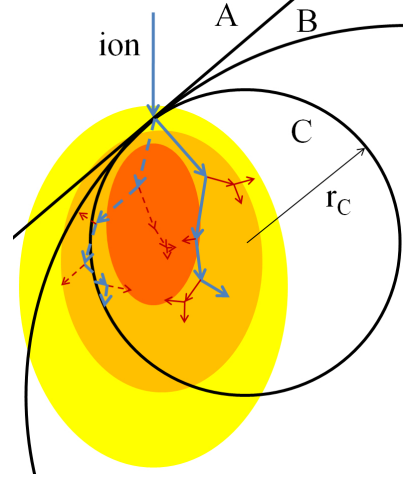
Figure 2.3: Illustration of the Sigmund model of sputtering for irradiation of a bulk sample at an angle θ . The ion enters the target at the point O and deposits energy by nuclear stopping as indicated by the oval contours. The energy deposited along the inclined surface $B'A'$ is larger than that for the perpendicular surface BA leading to increased sputtering for irradiation at an angle. Also the deposited energy and thus sputtering is not largest exactly at the point of incidence O, but further down at the point C. This is illustrated by the projection of the sputter yield 'S' onto the lateral dimension 'y'. Adapted from [Sig73].

With the situation illustrated in figure 2.3, the Sigmund theory can explain surface roughening by ion bombardment. For example, the Bradley-Harper theory of ripple formation on ion irradiated planes relies on the anisotropic sputtering predicted by the Sigmund model applied to a structured surface [Sig73, BH88]. The increased sputtering at a point (C), downstream from the point where the ion enters the target (O), leads to an enhancement of surface roughness.

The Sigmund theory can also be applied to curved surfaces. For nano-sized spheres or cylinders, the Sigmund theory can be invoked to predict that the sputter yield will be maximum when the ion range is comparable to the nanostructure diameter. Consider sputtering for a fixed ion energy and a varying diameter, illustrated in figure 2.4. At extremely large

2 Background

Figure 2.4: Illustration of the Sigmund model of sputtering for irradiation of a curved surface. For an infinite curvature radius (straight line A) a non-central impact is the same as irradiation at an angle, as shown in figure 2.3. For decreasing radii (B) the intersection between the colored energy distribution and the surface is increased. For small radii (r_C , C) forward sputtering appears. Two exemplary ion paths contributing to the colored average energy distribution are shown. The dashed path leaves and returns to the smallest structure C.



diameters atoms can only be sputtered from the flat surface (A in figure 2.4) facing the ion beam. The sputter yield will still be larger than for an unstructured bulk sample as the local angle of irradiation is increased for non central impacts. For decreasing diameters the curvature of the nanostructure increases, further increasing the intersection area between the estimated energy distribution and the nanostructure (B in figure 2.4). Once the diameter is in the order of the ion range, ‘forward’ sputtering along the direction of the ions initial path becomes possible (C in figure 2.4). There is a maximum sputter yield for a radius comparable to the ion range, because the total surface area shrinks as $1/r^2$, reducing the sputter yield again for decreasing diameters.

This model is obviously limited, as the energy distribution is assumed to remain constant even if it is intersected by the target surface (dashed lines in figure 2.3). The maximum in the Gaussian ellipsoid approximation of the mean energy deposition is found where many of the branches of collision cascades overlap. A constant distribution wrongly includes those ion paths that would have left the nanostructure, as shown by the dashed ion trajectory in figure 2.4. Thus, a more detailed description of the process is required.

2.2 Simulation of ion-solid interaction

In practice, the theory of ion-solid interactions is implemented in simulation tools, which allow the experimenter to predict experimental outcomes. Most frequently the energy dependence of the ion range is obtained by such simulations and used to decide which ion energy and ion fluence of irradiation is needed to create a desired doping concentration profile. On a more fundamental level, an experimentally observed behavior can be understood better by comparing it to various simulations to discern the dominating effects. The two main simulation approaches used for the ion-solid interactions are Monte-Carlo (MC) and molecular dynamic simulations (MD), both outlined in the following sections. Two dated, but highly recommendable reviews on the topic are given in references [And86, Eck91].

Monte-Carlo simulations

Monte-Carlo codes are simulation codes that use random numbers for simulations. After numerous simulations with different randomized outcomes, a statistical approximation of the likely outcome can be derived. With the BCA, the solid ion-interaction lends itself very well to MC simulation, as the evolution of a collision cascade can be simulated by following the paths of the ion and all recoils reiteratively from one collision event to the next. The probability of a collision can be determined from the cross-sections determined by the interaction potential between the projectile and the atoms in the target. According to this probability, a randomized distance traveled in a straight line by the projectile is determined. The particle's kinetic energy is reduced by the electronic energy loss accordingly. This has the underlying assumption of a 'random material' and crystal structure effects such as channeling are not reproduced by such a simulation. Two further random numbers are used to determine the impact parameter and azimuthal angle. The trajectories of the projectile and target atom in the plane of impact after the impact

2 Background

are determined by this impact parameter, the interaction potential and the particle energy, as shown in figure 2.2.

Examples of simulation codes implementing this approach in planar targets are TRIDYN [ME84], SDTrimSP [BMS⁺08], corteo [Sch08], COS-IP0 [Hau84] and, by far the most popular, SRIM [Zie12]. The target composition is treated dynamically in TRIDYN and SDTrimSP, changing with the incorporation of ions and with selective sputtering of target atoms and the incorporated ions. It is clear from the discussion of chapter 2.1 and figure 2.4 that the irradiation of a nanostructure can not be approximated well with a planar simulation. Therefore, the recently developed TRI3DYN [Mö14] and *iradina* [BR11] run a BCA MC simulation in a volume subdivided into rectangular voxels containing either vacuum or material to represent a three dimensional, structured target. TRI3DYN even includes dynamic composition and structural relaxation during the irradiation on a three dimensional simulation volume, but unfortunately it is not publicly available yet. Several *iradina* simulation results will be discussed in this thesis, so some points on the expected accuracy have to be made.

The advantage of MC BCA simulations in general is that the direct simulation of the ion trajectories gives an accurate prediction of the final distribution of the ions in the target. This is a result of the sufficient accuracy of the previously discussed underlying theory of the energy losses for high ion energies. These predominantly determine the distance traveled by the ion in a collision cascade and also the distribution of nuclear and electronic energy loss. As the simulation directly follows the ions path, this accuracy can be expected to be upheld in the irradiation of nanostructures, such as nanowires. The concentration of incorporated ions is somewhat lower in nanowires than in bulk targets, as in a nanowire there are more possible paths that lead to the ions being scattered out of the nanowire, than there are in the irradiation of a bulk surface, see chapter 2.1, figure 2.4 and reference [Bor12].

Predicting the damage caused in the material by nuclear energy loss is a much more difficult prospect. The *iradina* code checks at each collision

2.2 Simulation of ion-solid interaction

whether the target atom acquires more energy than the “displacement energy” which is a material specific parameter. If an atom has less than the displacement energy after a collision, it is assumed to remain bound in its place and the energy is converted into phonons. Atoms with more energy are displaced, creating a Frenkel pair which is counted as an interstitial at the location where the atom finally comes to rest and a vacancy at its point of origin. The displacement energy is experimentally accessible for crystalline materials by electron irradiation experiments in which the irradiating electron energy is in the order of MeV [CW65]. From the electrons’ impulse and mass the maximum transferred energy can be calculated. The defects produced as a function of electron energy can thus be used to determine a threshold energy transfer for the creation of point defects, and this value is defined as the displacement energy. This not possible for amorphous materials, where point defects are ill-defined. Also, the number of Frenkel pairs is only an estimation at the *creation rate* of the defects. The critical role that defect mobility, agglomeration and annealing plays in ion irradiation, especially at elevated temperatures, is totally neglected [PMB04, Nor14].

Better results can be expected for the computation of sputtering by MC simulation tools, for which an excellent review is given in reference [Bie87]. The difficulty is that for low projectile energies the interaction with both the nuclear and the electronic system are not generalizable, as discussed in chapter 2.1. This is a problem, as the dominating contribution to sputtering is made by low energy recoils [Tho68]. The various relevant interaction potentials, however, differ most at low energies. In addition, the SBE model used for Sigmund sputtering is just an approximation of the complexities arising at real surfaces. For metals the situation is most favorable and in reference [Bie87] sputter yields of various metals are reproduced quantitatively. More recently, in reference [HZM14] by Hofsäss et al., good results on the sputtering of *Si* and *Ge* were obtained using the *Kr-C* [WHB77] potential which was found to be superior to the ZBL potential [ZLB85]. In *iradina* only the ZBL potential is implemented, however, neither the *Kr-C* nor the ZBL potential

2 Background

reproduce the angle dependent potential of covalently bonded solids such as *Si* [SW85, Ter88]. Radially symmetric potentials are always only an approximation and which potential provides the better approximation in which scenario is not generally clear.

Hofsäss et al. [HZM14] also report a change in the dependence of sputtering on the angle of incidence for different interaction potentials. This might be worrisome even for the qualitative dependencies in the irradiation of nanostructures investigated in this thesis. However, the effect of different potentials on angle dependent sputtering is caused by the change in the critical angle for scattering at the surface of the impinging ion, not by a later change in the distribution of the nuclear energy deposition within the target [EHF92]. Since the critical gracing incidence angle is close to 0° regardless of the interaction potential for the relatively high energies ($\approx 100 \text{ keV}$) used in this dissertation [YS84], the accuracy of qualitative predictions will be unaffected. Finally, Hofsäss et al. [HZM14] also compared reported experiments on the compounds Ta_2O_5 and SiO_2 with simulations, finding that composition changes, caused by preferential sputtering of one element in the compound, play a significant role. This makes dynamic simulations necessary. As this is not possible in *iradina*, it will be discussed where relevant.

Even though *iradina* can implement an analytical description of a cylinder [Bor12], most of the simulations in this work were performed on the voxel based simulation volume, as this granted more freedom in the creation of the simulation volumes. A typical simulation volume is shown in figure 2.5. The number of target atoms leaving the simulation volume per impinging ion gives the sputter yield. To ensure *iradina* accounts for the surface binding energy correctly, the outermost voxel of the simulation volume has to contain vacuum, so that a sputtered atom makes a material-to-vacuum transition inside the simulation volume. Where the axial distribution was not relevant, the voxel z -size was set to 10 nm with periodic boundary conditions. The accuracy of the approximation of a curved surface in the xy direction, such as the surface of the cylindrical nanowires, is obviously dependent on the voxel size. Since the surface of

2.2 Simulation of ion-solid interaction

the approximation by rectangular voxels of a cylinder is strictly larger than the analytical surface, sputtering may be slightly increased. Also, the possible ions' impact angles are limited to the angle between the ion beam and the plane surfaces of the voxels facing the ion beam, so that the impinging angle is always larger in the voxelated surface than for the analytical surface. However, this will have no large effect, since, as before, the small critical angles for reflection of ions are restricted to the very outermost edges of the nanowire. Considering these effects, it was found that for voxel edges of 2 nm and below only a negligible influence of the voxel size on the sputtering remained.

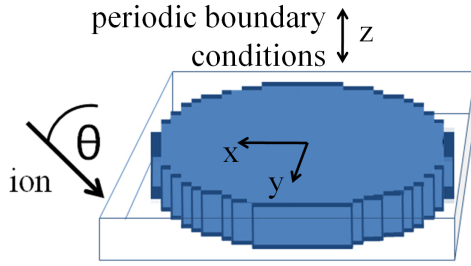


Figure 2.5: Typical implementation of a nanowire for an *iradina* simulation. The ions enter the simulation volume at $x = 0$; $y, z = \text{random}$ with an angle to the z -axis of $\theta = 45^\circ$. The x and y direction have 102 voxels of $0.02 - 2\text{ nm}$ edge-length so that nanowire with diameters of $2 - 200\text{ nm}$ can be simulated. The z -direction is periodically continued.

In summary, the prediction of sputtering as simulated by *iradina* in this thesis is expected to be dependable with respect to the qualitative relationship between ion range and structure size, and sputtering. Quantitative sputter yields will, however, be inaccurate.

Molecular dynamic simulations

The MC BCA simulations outlined so far inherently neglect all effects occurring when more than two particles move at the same time. Molecular dynamic (MD) simulations, however, follow the path of every particle in the simulation volume individually, calculating the interaction potential between them at every time step [AW59]. Obviously this is much more computationally expensive than the BCA and simulation volumes and times are thus limited. Nevertheless, the method can be applied

2 Background

to ion irradiation [Nor95] and increasing computer power has led to the simulation of ever higher particle energies, which require a larger simulation volume and time [GHB⁺13, BD14, ABU15]. The interactions between the target atoms in the MD simulations have to recreate the atomic structure, thermal vibrations etc., so that the low energy regime of the interaction potential is critical and has to be adapted to the specific problem [Ded95, NRS97, ANNK02, ND08]. Electronic energy loss can be included as a frictional force, however, treating this energy in a consistent manner is a problem, as the electronic system is typically not explicitly represented. Since MD simulations can reproduce the thermal evolution of a system, references to relevant MD simulation studies will be included in the discussion of results in this thesis.

Relevant simulations in literature

Two recent investigations on sputtering of spherical [NSUM14] and cylindrical [UBNM15] nanostructures have to be mentioned here as they overlap significantly with the studies made in this thesis. These publications have found the Sigmund model, as it was discussed in chapter 2.1, to be a decent first approximation for sputtering of nanostructures. They go on to compare the sputter yield results from MC and MD simulations and discuss its diameter dependence. Unfortunately, the nanowire diameters investigated by MD are quite small owing to the computational costs. They find that for decreasing nanostructure diameters sputtering of clusters and thermal evaporation become increasingly important due to the lower number of atoms amongst which the ion deposited energy is distributed. This dissertation adds to results of these studies with explicit simulations of diameter and energy dependent sputtering of nanowires in chapter ?? and an experimental investigation of this dependency in the following chapter ??.

3 Experimental Methods

3.1 Nanowire synthesis

Nanowire synthesis can be categorized according to two approaches: “bottom-up” and “top-down”. The “bottom-up” approach relies on the self-organized arrangement of matter using an inherent anisotropy in the growth mechanism to create nanoscale structures. Depending on the material, crystal quality, morphology, infrastructural requirements, the quantity to be produced etc. there is a large variety of processes available for synthesis. The *ZnO* [BMS⁺06, Sti08, Mü09, CZC⁺10, Ogr13] and *Si* [LSH⁺08] nanowires investigated in this dissertation were grown using vapor transport, pulsed laser deposition (PLD) and chemical vapor deposition (CVD) respectively.

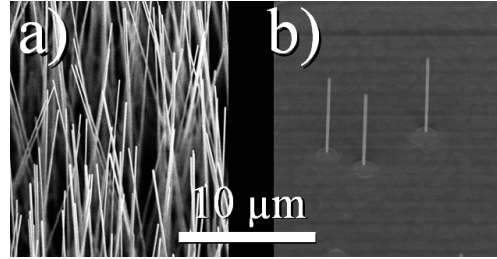
A very common mechanism to create the anisotropy required to get the one dimensional growth of nanowires is the vapor-liquid-solid growth (VLS) first described by Wagner and Ellis [WE64]. The growth of the “bottom-up” nanowires used in this thesis relies on the VLS mechanism. The variety of processes available for nanowire growth are responsible to provide the ‘vapor’ of material for this growth mechanism. With the vapor transport technique the source material eg. *ZnO* is simply evaporated in a typically inert atmosphere and transported within a reactor to the substrate by diffusion or gas flow. Chemical vapor deposition uses reactive gases such as *SiH₄* to provide the source material, in this case *Si* in a temperature and pressure controlled reactor.

Although self-catalyzed growth has also been observed, the liquid phase exploited in VLS is typically provided by a metal catalyst deposited on the growth substrate [DL00, WDJ⁺09]. The material in the

3 Experimental Methods

vapor phase can accumulate in the catalyst droplet until the concentration is supersaturated. Preferential segregation of the excess material at the droplet-substrate interface leads to the growth of a nanowire. The size of the droplet can be used to control the diameter of the grown nanowire to some extent. An epitaxial relation between the substrate and the nanowire material may be used to direct the growth. Typical nanowire diameters and lengths are $50 - 300\text{ nm}$ and $> 5\text{ }\mu\text{m}$ respectively.

Figure 3.1: SEM images of the ZnO nanowire samples. In a) the dense samples grown via vapor transport on AZO are shown, while b) shows the sparser, PLD grown ZnO nanowires on a sapphire substrate.



Relatively dense ZnO nanowire samples are grown by vapor transport in Jena in the three-zone-furnace (3ZJ). The nanowires grow upstanding on a $\approx 500\text{ nm}$ layer of Al doped ZnO (AZO) sputtered onto a Si substrate, as shown in figure 3.1a. The temperature at the 1 : 1 molar source mixture of ZnO and C was $1050\text{ }^\circ\text{C}$, the substrate position at 46 cm , Ar and O_2 flow 10 sccm each and the base pressure 7 mbar [BMS⁺06, Sti08, Mü09, Ogr13]. Further ZnO nanowire samples with a sparser lateral distribution of the upright nanowires on a sapphire substrate decorated with Au colloids are shown in figure 3.1b. They were kindly provided from the University of Leipzig by Dr. Helena Franke. The parameters for the PLD growth of these samples are a laser power density of 2 J/cm^2 , 165 mbar base pressure at 40 sccm Ar flow, a substrate temperature of $900\text{ }^\circ\text{C}$ and a target-substrate distance of 35 mm [CZC⁺10].

Nanowires can also be synthesized “top-down” [HIK97, HKZ⁺10]. A “top-down” approach requires a predefined template which is used to control the desired morphology. The Si -nanowire arrays used to study sputtering and plastic deformation within this dissertation were etched by reactive ion etching (RIE) through a circular, e-beam lithographically

3.2 Modification

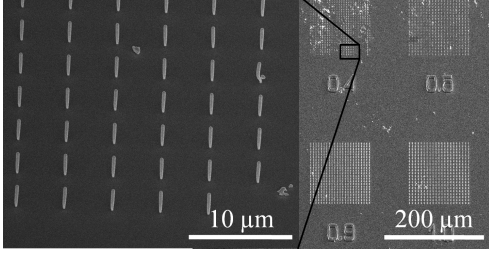


Figure 3.2: SEM images of the etched *Si* nanowire arrays. On the right, the numbers etched into the substrate under each array indicate the diameter in μm of the predefined *Ni* mask for that array.

defined *Ni* hard-mask which set the nanowire diameter [JNW⁺15]. The RIE parameters were a flow of 50 *sccm* SF_6 and 100 *sccm* O_2 at a set pressure of 10 *mTorr* and a strike pressure of 30 *mTorr*. The radio frequency and inductive coupled plasma powers were 15 *W* and 100 *W*, respectively. The etching was performed at $-108\text{ }^\circ\text{C}$ for 5-15 *min*. After the RIE process, a 32 % *HCl* and (7:1)-buffered *HF* dip removed the *Ni*-hard mask and the oxide formed at the surface of the *Si*, respectively. Using this “top-down” etching process it is possible to prepare nanowires with diameters varying from 50 *nm* to 2 μm with a height of $\approx 3\text{ }\mu m$ on a single substrate for simultaneous irradiation. As seen in figure 3.2, the spacing between the nanowires was larger than their height, so that there is no shadowing of the ion beam between the nanowires.

3.2 Modification

ROMEO

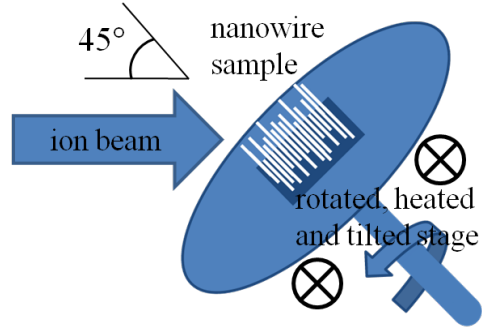
The ion irradiation for this dissertation was performed at the general purpose High Voltage Engineering implanter “ROMEO” at the IFK in Jena. It can provide an ion beam of virtually any element at energies ranging from 10 – 380 *keV*. The beam passes a 90° selector magnet and can be swepted with a frequency of $\approx 1\text{ kHz}$ to homogeneously irradiate areas up to several tens of cm^2 with ion currents of up to 1 *mA*. For this work ion current densities were limited to 500 nA/cm^2 , corresponding to $\approx 15\text{ min}$ for the typical fluence of $10^{16}\text{ ions}/cm^2$.

Previous work has shown that nanowires can bend under ion irradiation [BSL⁺11, Bor12]. Therefore, a rotatable, heatable and tilted stage

3 Experimental Methods

(RHT), illustrated in figure 3.3, was custom built within the frame of this thesis, together with Stefan Noack [Noa14]. With it, bending of the upstanding nanowires can be avoided as the nanowires are irradiated homogeneously from all sides at an angle of 45° . All the samples investigated in this thesis were rotated on the RHT and its preceding prototype sample stages during the irradiation.

Figure 3.3: *RHT Foto* Illustration of the rotated, heated and tilted (RHT) stage for the ROMEO implanter. The rotating stage is tilted towards the ion beam by 45° and heated from the back by two light bulbs. The temperature is controlled by a reference measurement on a stationary disk similar to the rotating stage.



The sputtering and plastic deformation studies in chapters ?? and ?? were conducted with Ar^+ irradiation in Si nanowires to avoid any chemical effects of the incorporated ions. To prevent defect induced density changes and the Si nanowires from amorphizing, the irradiation temperature was 300° for the sputtering study. At this temperature the amorphization threshold becomes arbitrarily high [PMB04]. The other irradiations were performed at room-temperature. For the quantification of dopants in chapter ??, ZnO -nanowires were irradiated with Mn^+ . Mn has a similar mass to Zn and both are medium-weight so that the linear cascade theory is applicable. Also, $ZnO : Mn$ is interesting as a possible material for diluted magnetic semiconductors (DMS) [Fur88, NKA⁺04]. Pragmatically, it is relatively easy to get a stable Mn^+ beam with ROMEO and with the quantification in mind, Mn is much less likely to be in any components at the XRF beamline and give a background than Fe, Co, Ni or Cu .

Focused ion beam - FIB

Some sample preparations required a FIB. These are highly specialized ion accelerators with the main objective of obtaining a small ion beam focus. Most of the systems use a Ga^+ beam and acceleration voltages up to 30 keV . The main use for FIBs is to sputter material extremely locally, making it a versatile tool for nano-machining. The FEI DualBeam Helios NanoLab 600i FIB system used for this dissertation is a scanning electron microscope (SEM) - FIB combination. The sample can thus be milled with the ion beam and investigated with the SEM reiteratively. The system is also equipped with a Pt -metal-organic gas injection system. The Pt containing organic molecule can be cracked locally on the sample by the secondary electrons created by either the electron or ion beam. Most of the Pt is deposited near the impact point of the primary beam at the substrate. However, typically a rather large ‘halo’ of minor Pt deposition can extend for a couple of μm . The FIB system can thus mill and deposit structures on a nm scale. For the sample preparation in this thesis all Pt deposition was done with the electron beam to avoid damage to the nanowire by the Ga^+ ion beam.

3.3 Characterization

Scanning Electron Microscope - SEM

The morphological changes in the nanowires were characterized by high resolution SEM in the FEI DualBeam Helios NanoLab 600i FIB system. The lateral resolution of the SEM system is $\approx 2\text{ nm}$. Images of individual nanowires were made before and after ion irradiation to quantify the sputtering. To find exactly the same place on the sample, a series of images with increasing magnification has to be made. Typically, images were made at an angle of 45° to the substrate with the alignment procedure the same before and after irradiation.

A semi-automated image analysis protocol was developed by Stefan Noack in his Master thesis [Noa14, JNW⁺15] to evaluate the SEM im-

3 Experimental Methods

ages of a large number of nanowires. It applies a (3x3) median filter to smooth out some noise and a Gaussian unsharp mask with $\sigma = 1\text{ px}$ and weighted at 60 % to resharpen the edges [San04]. An Otsu threshold [Ots79] is applied to separate the brighter nanowire from the darker background. Next, open source particle analysis software is used to find the main body of the nanowire and turn it upright, correcting any marginal tilt remaining in the SEM images [SACF⁺12, SPTS12]. Finally the sum of the gray-values in each line is used to calculate the diameter at that height along the nanowire axis. As the investigated nanowires showed a characteristic bulge at the base, this point was used to align the height profiles of a single wire before and after irradiation. To avoid any irregular effects by the altered geometry at the top facet and the base of the nanowire, $\approx 20\%$ of the height was disregarded at either end of the extracted profile. After a fluence of 10^{16} cm^{-2} the change in diameter was close to the resolution limit of the SEM, therefore only the data for two subsequent irradiation steps of $2 \cdot 10^{16}\text{ cm}^{-2}$ ions was evaluated. A more detailed description of the image analysis process can be found in reference [Noa14] and the supplementary information of reference [JNW⁺15].

Electron Back-Scatter Diffraction - EBSD

A Carl Zeiss Auriga CrossBeam Workstation fitted with an EBSD tool was used to identify whether nanowires remained crystalline after irradiation. The electron beam is focused on the sample at an arbitrary angle and the scattered electrons are detected by a large CCD detector in the SEM. Bragg diffraction along the crystal lattice planes produces a characteristic pattern of Kikuchi lines on the detector [Kik28, FH13] in crystalline samples. Amorphous or nano-crystalline samples show no pattern.

nano-XRF

Hard X-ray radiation stimulates the atoms within the radiated material to emit characteristic X-ray radiation. This X-ray fluorescence can be detected in an energy dispersive semiconductor detector and used to identify and quantify the elements in the sample [?]. In principle the method is similar to the more wide-spread energy dispersive X-ray spectroscopy (EDX), where an electron beam is used to excite characteristic X-ray fluorescence [?]. Very good lateral resolution can be obtained by having an EDX detector in a SEM. However, the advantage of using X-rays lies in the absence of Bremsstrahlung which high energy electrons produce in matter in addition to characteristic X-rays. In XRF there is thus a much lower background and much lower concentrations of elements can be detected and quantified. Unlike normal X-ray tubes, synchrotron radiation is very brilliant, allowing it to be focused.

X-ray fluorescence with a nano-focussed X-ray beam (nano-XRF) was measured at the European Synchrotron Radiation Facility (ERSF), beamlines ID16b and ID13. The beamlines were run at various photon energies above 15 keV and with focal spot of typically $\approx 80\text{ nm}$ and $\approx 250\text{ nm}$ diameter, respectively. The nano-XRF thus allows the quantification of low concentrations with sufficient lateral resolution to resolve axial concentration gradients in a nanowire. Unfortunately, the resolution is not high enough to investigate radial distributions.

For this thesis, Mn irradiated ZnO nanowires were deposited on TEM grids either randomly by ‘imprinting’ or individually by using the manipulator in the FEI DualBeam FIB. Transferring individual wires requires some finesse, but it is possible to detach ZnO nanowires from their substrate without the Ga^+ FIB and to place them on the “lacey-carbon” TEM grids without any additional Pt deposition. In this way SEM images before and after irradiation of the same wire investigated by nano-XRF are available. At both beamlines the nanowires on the TEM grids are scanned under the fixed focal point of the X-ray beam

3 *Experimental Methods*

with piezo-motors while the XRF spectra are collected with a Vortex EM silicon drift X-ray detector.

The spectra used for quantification were obtained in multiple scans across a nanowire at regular intervals along the its length. As the XRF signal can be used to locate the nanowire, only the points near the nanowire were measured with a high integration time and a low step-with ($< 1/2$ focal spot) to ensure a large number of counts ($> 10^5$ per scan) at reasonable measuring times.

nano-XRF quantification

The XRF-Spectra were evaluated using the open source PyMCA software package [SPC⁺07]. The effects of self absorption and excitation can be neglected, as the investigated nanowires are very thin compared to the X-ray absorption length, which is a couple of μm in ZnO . However, the detector-sample distance is responsible for an unavoidable attenuation length in air. Here, the X-ray absorption is dominated by Ar . As Mn is relatively light, its characteristic X-ray emission at $K_{\alpha, Mn} = 5.9 keV$ is absorbed more than the signal of the heavier Zn with $K_{\alpha, Zn} = 8.6 keV$. Thus, absorption of the XRF signal in air has to be considered carefully in the fitting with PyMCA. The accuracy was double checked by measuring and quantifying trace elements in a calibration sample of bovine liver. In this way, optimal fitting parameters were found for each beam-time and applied to the respective spectra in the PyMCA batch mode.

Oxygen cannot be quantified in these beamlines, as its XRF emission is totally attenuated by air and a Si dead layer in the detector. The quantification of the Mn content in the ZnO nanowires thus relies on the assessment of the Mn/Zn ratio. In any case, it is a decent approximation to assume that the ZnO remains stoichiometric even during the irradiation. The samples are irradiated in a chamber with a base pressure $\approx 10^{-6} mbar$, so according to the Hertz-Knudsen equation this will give a coverage of roughly one mono-layer or $10^{15} particles/cm^2s$, if one assumes a sticking coefficient near 1. The maximum ion current density yields $10^{13} ions/cm^2s$, so that an unlikely amount of preferential sputtering would be required to deplete the oxygen out of the wires. In addition, the wires will be oxidized in the normal atmosphere post irradiation. The Mn/Zn ratio is thus a good proxy for the Mn concentration.

The quantification limit can be estimated using a simulated XRF spectrum from PyMCA. By finding an appropriate photon flux and nanowire interaction volume, the simulation can reproduce the XRF spectrum with the actually measured number of counts at $K_{\alpha, Zn}$. The Mn content in the simulated matrix can then be decreased until the minimum Mn

3 *Experimental Methods*

content is found which gives a signal at $K_{\alpha,Mn}$ just above the actually measured noise level. In this way a lower limit for the concentration resolution can be found at typically 0.1 % Mn/Zn .

4 Summary and Outlook

check: Master Thesis Noack, Ogrisek, Conference proceeding D. Sage, Rutherford, Nordlund

Bibliography

- [ABU15] Christian Anders, Eduardo M. Bringa, and Herbert M. Urbassek. Sputtering of a metal nanofoam by Au ions. *Nuclear Instruments and Methods in Physics Research Section B: Beam Interactions with Materials and Atoms*, 342:234–239, January 2015. 00000.
- [And86] Hans Henrik Andersen. Computer simulations of atomic collisions in solids with special emphasis on sputtering. *Nuclear Instruments and Methods in Physics Research Section B: Beam Interactions with Materials and Atoms*, 18(1-6):321–343, January 1986.
- [ANNK02] Karsten Albe, Kai Nordlund, Janne Nord, and Antti Kuroonen. Modeling of compound semiconductors: Analytical bond-order potential for Ga, As, and GaAs. *Physical Review B*, 66(3):035205, July 2002.
- [ASS69] Hh Andersen, H. Simonsen, and H. Sorensen. An Experimental Investigation of Charge-Dependent Deviations from Bethe Stopping Power Formula. *Nuclear Physics A*, A125(1):171–&, 1969. WOS:A1969C725100012.
- [AW59] B. J. Alder and T. E. Wainwright. Studies in Molecular Dynamics. I. General Method. *The Journal of Chemical Physics*, 31(2):459–466, August 1959. 01183.
- [BD14] Richard E. Baumer and Michael J. Demkowicz. Prediction of Spontaneous Plastic Deformation of Irradiated Metallic

- Glasses due to Thermal Spike-Induced Plasticity. *Materials Research Letters*, 2(4):221–226, October 2014.
- [Bet30] H. Bethe. Zur Theorie des Durchgangs schneller Korpuskularstrahlen durch Materie. *Annalen der Physik*, 397(3):325–400, January 1930.
- [BH88] R. Mark Bradley and James M. E. Harper. Theory of ripple topography induced by ion bombardment. *Journal of Vacuum Science & Technology A*, 6(4):2390–2395, July 1988.
- [Bie87] J. P. Biersack. Computer simulations of sputtering. *Nuclear Instruments and Methods in Physics Research Section B: Beam Interactions with Materials and Atoms*, 27(1):21–36, June 1987.
- [Blo33] F. Bloch. Zur Bremsung rasch bewegter Teilchen beim Durchgang durch Materie. *Annalen der Physik*, 408(3):285–320, January 1933.
- [BMB⁺11] Christian Borschel, Maria E. Messing, Magnus T. Borgstrom, Waldomiro Paschoal, Jesper Wallentin, Sandeep Kumar, Kilian Mergenthaler, Knut Deppert, Carlo M. Canali, Hakan Pettersson, Lars Samuelson, and Carsten Ronning. A New Route toward Semiconductor Nanospintronics: Highly Mn-Doped GaAs Nanowires Realized by Ion-Implantation under Dynamic Annealing Conditions. *Nano Letters*, 11(9):3935–3940, September 2011. WOS:000294790200073.
- [BMS⁺06] C. Borchers, S. Müller, D. Stichtenoth, D. Schwen, and C. Ronning. Catalyst Nanostructure Interaction in the Growth of 1d ZnO Nanostructures. *The Journal of Physical Chemistry B*, 110(4):1656–1660, February 2006.
- [BMS⁺08] Ivan Bizyukov, Andreas Mutzke, Ralf Schneider, Alexander M. Gigler, and Karl Krieger. Morphology and changes of

Bibliography

- elemental surface composition of tungsten bombarded with carbon ions. *Nuclear Instruments and Methods in Physics Research Section B: Beam Interactions with Materials and Atoms*, 266(9):1979–1986, May 2008. 00007.
- [Bor12] Christian Borschel. *Ion-Solid Interaction in Semiconductor Nanowires*. PhD thesis, University Jena, Jena, 2012.
- [BR11] C. Borschel and C. Ronning. Ion beam irradiation of nanostructures – A 3d Monte Carlo simulation code. *Nuclear Instruments and Methods in Physics Research Section B: Beam Interactions with Materials and Atoms*, 269(19):2133–2138, October 2011.
- [BSL⁺11] Christian Borschel, Susann Spindler, Damiana Leroose, Arne Bochmann, Silke H. Christiansen, Sandor Nietzsche, Michael Oertel, and Carsten Ronning. Permanent bending and alignment of ZnO nanowires. *Nanotechnology*, 22(18):185307, May 2011. WOS:000288653300010.
- [CW65] J. W. Corbett and G. D. Watkins. Production of Divacancies and Vacancies by Electron Irradiation of Silicon. *Physical Review*, 138(2A):A555–A560, April 1965.
- [CZC⁺10] B. Q. Cao, J. Zuniga-Perez, C. Czekalla, H. Hilmer, J. Lenzner, N. Boukos, A. Travlos, M. Lorenz, and M. Grundmann. Tuning the lateral density of ZnO nanowire arrays and its application as physical templates for radial nanowire heterostructures. *Journal of Materials Chemistry*, 20(19):3848–3854, May 2010.
- [Ded95] Gv Dedkov. The Interatomic Interaction Potentials in Radiation Physics. *Physica Status Solidi a-Applications and Materials Science*, 149(2):453–513, June 1995. WOS:A1995RH61400001.

- [Dha07] S. Dhara. Formation, dynamics, and characterization of nanostructures by ion beam irradiation. *Critical Reviews in Solid State and Materials Sciences*, 32(1-2):1–50, 2007. WOS:000247237500001.
- [DL00] X. Duan and C. M. Lieber. General Synthesis of Compound Semiconductor Nanowires. *Advanced Materials*, 12(4):298–302, February 2000.
- [Eck91] Wolfgang Eckstein. *Computer Simulation of Ion-Solid Interactions*. Springer Berlin Heidelberg, Berlin, Heidelberg, 1991.
- [EHHF92] W. Eckstein, S. Hackel, D. Heinemann, and B. Fricke. Influence of the Interaction Potential on Simulated Sputtering and Reflection Data. *Zeitschrift Fur Physik D-Atoms Molecules and Clusters*, 24(2):171–176, September 1992. WOS:A1992JQ04000013.
- [FH13] Brent Fultz and James Howe. *Transmission Electron Microscopy and Diffractometry of Materials*. Graduate Texts in Physics. Springer Berlin Heidelberg, Berlin, Heidelberg, 2013.
- [Fur88] J. K. Furdyna. Diluted magnetic semiconductors. *Journal of Applied Physics*, 64(4):R29–R64, August 1988.
- [GHB⁺13] G. Greaves, J. A. Hinks, P. Busby, N. J. Mellors, A. Ilinov, A. Kuronen, K. Nordlund, and S. E. Donnelly. Enhanced Sputtering Yields from Single-Ion Impacts on Gold Nanorods. *Physical Review Letters*, 111(6):065504, August 2013. 00004.
- [GS28] R. Glocker and H. Schreiber. Quantitative Röntgenspektralanalyse mit Kalterregung des Spektrums. *Annalen der Physik*, 390(8):1089–1102, January 1928.

Bibliography

- [Hau84] M. Hautala. Nuclear stopping in polycrystalline materials: Range distributions and Doppler-shift attenuation analysis. *Physical Review B*, 30(9):5010–5018, November 1984. 00059.
- [HFH⁺90] S. Hackel, B. Fricke, D. Heinemann, D Kolb, and L Yang. Inter-Nuclear Potential of the System Si-Si calculated with the Finite-Element-Method. *GSI Annual Report*, page 165, 1990.
- [HIK97] C. Haginoya, M. Ishibashi, and K. Koike. Nanostructure array fabrication with a size-controllable natural lithography. *Applied Physics Letters*, 71(20):2934–2936, November 1997. WOS:A1997YF67500022.
- [HKZ⁺10] Birgit J. M. Hausmann, Mughees Khan, Yinan Zhang, Tom M. Babinec, Katie Martinick, Murray McCutcheon, Phil R. Hemmer, and Marko Loncar. Fabrication of diamond nanowires for quantum information processing applications. *Diamond and Related Materials*, 19(5-6):621–629, June 2010. WOS:000278193600059.
- [HZM14] H. Hofsäss, K. Zhang, and A. Mutzke. Simulation of ion beam sputtering with SDTrimSP, TRIDYN and SRIM. *Applied Surface Science*, 310:134–141, August 2014.
- [JHMR15] Andreas Johannes, Henry Holland-Moritz, and Carsten Ronning. Ion beam irradiation of nanostructures: sputtering, dopant incorporation, and dynamic annealing. *Semiconductor Science and Technology*, 30(3):033001, March 2015.
- [JNW⁺15] Andreas Johannes, Stefan Noack, Werner Wesch, Markus Glaser, Alois Lugstein, and Carsten Ronning. Anomalous Plastic Deformation and Sputtering of Ion Irradiated Silicon Nanowires. *Nano Letters*, May 2015.
- [Jon24] J. E. Jones. On the Determination of Molecular Fields. II. From the Equation of State of a Gas. *Proceedings of the*

Royal Society of London A: Mathematical, Physical and Engineering Sciences, 106(738):463–477, October 1924.

- [JS82] W. Jansen and M. Slaughter. Elemental Mapping of Minerals by Electron Micro-Probe. *American Mineralogist*, 67(5-6):521–533, 1982. WOS:A1982NZ59500008.
- [Kik28] Seishi Kikuchi. Diffraction of Cathode Rays by Mica. *Proceedings of the Imperial Academy*, 4(6):271–274, 1928.
- [KPJ⁺13] Sandeep Kumar, Waldomiro Paschoal, Andreas Johannes, Daniel Jacobsson, Christian Borschel, Anna Pertsova, Chih-Han Wang, Maw-Kuen Wu, Carlo M. Canali, Carsten Ronning, Lars Samuelson, and Håkan Pettersson. Magnetic Polarons and Large Negative Magnetoresistance in GaAs Nanowires Implanted with Mn Ions. *Nano Letters*, 13(11):5079–5084, 2013.
- [Lin54] J. Lindhard. On the Properties of a Gas of Charged Particles. *Matematisk-Fysiske Meddelelser Kongelige Danske Videnskabernes Selskab*, 28(8):1–57, 1954. WOS:A1954XZ29300001.
- [LSH⁺08] A. Lugstein, M. Steinmair, Y. J. Hyun, G. Hauer, P. Pongratz, and E. Bertagnolli. Pressure-induced orientation control of the growth of epitaxial silicon nanowires. *Nano Letters*, 8(8):2310–2314, August 2008. WOS:000258440700034.
- [Mü09] Sven Müller. *Structural and optical impact of transition metal implantation into zinc oxide single crystals and nanowires*. PhD thesis, Georg-August Universität Göttingen, Göttingen, 2009.
- [Mö14] Wolfhard Möller. TRI3dyn – Collisional computer simulation of the dynamic evolution of 3-dimensional nanostructures under ion irradiation. *Nuclear Instruments and*

Bibliography

- Methods in Physics Research Section B: Beam Interactions with Materials and Atoms*, 322:23–33, March 2014. 00001.
- [ME84] W. Möller and W. Eckstein. Tridyn — A TRIM simulation code including dynamic composition changes. *Nuclear Instruments and Methods in Physics Research Section B: Beam Interactions with Materials and Atoms*, 2(1–3):814–818, March 1984.
- [MK97] Antonio Miotello and Roger Kelly. Revisiting the thermal-spike concept in ion-surface interactions. *Nuclear Instruments and Methods in Physics Research Section B: Beam Interactions with Materials and Atoms*, 122(3):458–469, February 1997.
- [Mol47] G. Moliere. Theorie Der Streuung Schneller Geladener Teilchen .1. *Zeitschrift Fur Naturforschung Section a-a Journal of Physical Sciences*, 2(3):133–145, 1947. WOS:A1947UW40000002.
- [Nas08] Nastasi/Mayer/Hirvonen. *Ion-Solid Interactions: Fundamentals and Applications*. Cambridge University Press, Cambridge ; New York, auflage: revised. edition, January 2008.
- [ND08] Kai Nordlund and Sergei L. Dudarev. Interatomic potentials for simulating radiation damage effects in metals. *Comptes Rendus Physique*, 9(3–4):343–352, April 2008.
- [NKA⁺04] Nick S. Norberg, Kevin R. Kittilstved, James E. Amonette, Ravi K. Kukkadapu, Dana A. Schwartz, and Daniel R. Gamelin. Synthesis of Colloidal Mn²⁺:ZnO Quantum Dots and High-TC Ferromagnetic Nanocrystalline Thin Films. *Journal of the American Chemical Society*, 126(30):9387–9398, August 2004.

- [Noa14] Stefan Noack. *Sputter Effects of Silicon Nanowires under Ion Bombardment*. University Jena, Master Thesis, 2014.
- [Nor95] K. Nordlund. Molecular dynamics simulation of ion ranges in the 1–100 keV energy range. *Computational Materials Science*, 3(4):448–456, March 1995. 00248.
- [Nor14] Kai Nordlund. Correction to the Kinchin-Phase damage equation to account for athermal defect recombination and ion beam mixing: arc-dpa and rpa. In *Oral Presentation*, Leuven, September 2014.
- [NRS97] K. Nordlund, N. Runeberg, and D. Sundholm. Repulsive interatomic potentials calculated using Hartree-Fock and density-functional theory methods. *Nuclear Instruments & Methods in Physics Research Section B-Beam Interactions with Materials and Atoms*, 132(1):45–54, October 1997. WOS:A1997YF32200007.
- [NSUM14] Maureen L. Nietiadi, Luis Sandoval, Herbert M. Urbassek, and Wolfhard Möller. Sputtering of Si nanospheres. *Physical Review B*, 90(4):045417, July 2014.
- [Ogr13] Matthias Ogrisek. *Kontrolliertes Wachstum von Zinkoxid und Vanadium(IV)-oxid Nanodrähten*. University Jena, Master Thesis, 2013.
- [Ots79] NOBUYUKI Otsu. A Threshold Selection Method from Gray-Level Histograms. *IEEE Transactions on Systems, Man, and Cybernetics*, 9(1):62–66, 1979.
- [PKB⁺12] Waldomiro Paschoal, Sandeep Kumar, Christian Borschel, Phillip Wu, Carlo M. Canali, Carsten Ronning, Lars Samuelson, and Hakan Pettersson. Hopping Conduction in Mn Ion-Implanted GaAs Nanowires. *Nano Letters*, 12(9):4838–4842, September 2012. WOS:000308576000069.

Bibliography

- [PKJ⁺14] W. Paschoal, Sandeep Kumar, D. Jacobsson, A. Johannes, V. Jain, C. M. Canali, A. Pertsova, C. Ronning, K. A. Dick, L. Samuelson, and H. Pettersson. Magnetoresistance in Mn ion-implanted GaAs:Zn nanowires. *Applied Physics Letters*, 104(15):153112, April 2014. WOS:000335145200060.
- [PMB04] Lourdes Pelaz, Luis A. Marqués, and Juan Barbolla. Ion-beam-induced amorphization and recrystallization in silicon. *Journal of Applied Physics*, 96(11):5947–5976, December 2004.
- [Rut11] E Rutherford. The scattering of alpha and beta particles by matter and the structure of the atom. *Philosophical Magazine Series 6*, 21(125):669–688, May 1911.
- [SACF⁺12] Johannes Schindelin, Ignacio Arganda-Carreras, Erwin Frise, Verena Kaynig, Mark Longair, Tobias Pietzsch, Stephan Preibisch, Curtis Rueden, Stephan Saalfeld, Benjamin Schmid, Jean-Yves Tinevez, Daniel James White, Volker Hartenstein, Kevin Eliceiri, Pavel Tomancak, and Albert Cardona. Fiji: an open-source platform for biological-image analysis. *Nature Methods*, 9(7):676–682, June 2012.
- [San04] B Sankur. Survey over image thresholding techniques and quantitative performance evaluation. *Journal of Electronic Imaging*, 13(1):146, January 2004.
- [SBB53] Fm Smith, W. Birnbaum, and Wh Barkas. Measurements of Meson Masses and Related Quantities. *Physical Review*, 91(3):765–766, 1953. WOS:A1953UB46200058.
- [Sch08] François Schiettekatte. Fast Monte Carlo for ion beam analysis simulations. *Nuclear Instruments and Methods in Physics Research Section B: Beam Interactions with Materials and Atoms*, 266(8):1880–1885, April 2008.

- [Sig69] Peter Sigmund. Theory of Sputtering. I. Sputtering Yield of Amorphous and Polycrystalline Targets. *Physical Review*, 184(2):383–416, August 1969. 03204.
- [Sig73] Peter Sigmund. A mechanism of surface micro-roughening by ion bombardment. *Journal of Materials Science*, 8(11):1545–1553, November 1973.
- [Sig04] Peter Sigmund, editor. *Stopping of Heavy Ions*, volume 204 of *Springer Tracts in Modern Physics*. Springer Berlin Heidelberg, Berlin, Heidelberg, 2004.
- [SPC⁺07] V. A. Solé, E. Papillon, M. Cotte, Ph. Walter, and J. Susini. A multiplatform code for the analysis of energy-dispersive X-ray fluorescence spectra. *Spectrochimica Acta Part B: Atomic Spectroscopy*, 62(1):63–68, January 2007.
- [SPTS12] Daniel Sage, D. Prodanov, J.-Y. Tinevez, and J. Schindelin. ImageJ User & Developer Conference (IUDC’12). 2012.
- [SS14] Peter Sigmund and Andreas Schinner. Notes on the Barkas-Andersen effect. *European Physical Journal D. Atomic, Molecular, Optical and Plasma Physics*, 68, 2014.
- [Sti08] Daniel Stichtenoth. *Dimensionseffekte in Halbleiternanodrähten*. PhD thesis, Georg-August Universität Göttingen, Göttingen, 2008.
- [SW85] Frank H. Stillinger and Thomas A. Weber. Computer simulation of local order in condensed phases of silicon. *Physical Review B*, 31(8):5262–5271, April 1985.
- [TDP92] M. Toulemonde, C. Dufour, and E. Paumier. Transient thermal process after a high-energy heavy-ion irradiation of amorphous metals and semiconductors. *Physical Review B*, 46(22):14362–14369, December 1992.

Bibliography

- [Ter88] J. Tersoff. New empirical approach for the structure and energy of covalent systems. *Physical Review B*, 37(12):6991–7000, April 1988.
- [Tho68] Mw Thompson. Energy Spectrum of Ejected Atoms During High Energy Sputtering of Gold. *Philosophical Magazine*, 18(152):377–&, 1968. WOS:A1968B525400015.
- [UBNM15] Herbert M. Urbassek, R. Mark Bradley, Maureen L. Nettiadi, and Wolfhard Möller. Sputter yield of curved surfaces. *Physical Review B*, 91(16):165418, April 2015.
- [WDJ⁺09] Brent A. Wacaser, Kimberly A. Dick, Jonas Johansson, Magnus T. Borgström, Knut Deppert, and Lars Samuelson. Preferential Interface Nucleation: An Expansion of the VLS Growth Mechanism for Nanowires. *Advanced Materials*, 21(2):153–165, January 2009.
- [WE64] Rs Wagner and Wc Ellis. Vapor-Liquid-Solid Mechanism of Single Crystal Growth (New Method Growth Catalysis from Impurity Whisker Epitaxial + Large Crystals Si E). *Applied Physics Letters*, 4(5):89–&, 1964. WOS:A19645163A00003.
- [WHB77] W. D. Wilson, L. G. Haggmark, and J. P. Biersack. Calculations of nuclear stopping, ranges, and straggling in the low-energy region. *Physical Review B*, 15(5):2458–2468, March 1977.
- [Wie88] E Wiedemann. Über Fluoreszenz und Phosphoreszenz, I. Abhandlung. *Annalen der Physik*, 34:446–463, 1888.
- [WKW04] W. Wesch, A. Kamarou, and E. Wendler. Effect of high electronic energy deposition in semiconductors. *Nuclear Instruments & Methods in Physics Research Section B-Beam Interactions with Materials and Atoms*, 225(1-2):111–128, August 2004. WOS:000223792600010.

Bibliography

- [WWS12] W. Wesch, E. Wendler, and C. S. Schnohr. Damage evolution and amorphization in semiconductors under ion irradiation. *Nuclear Instruments and Methods in Physics Research Section B: Beam Interactions with Materials and Atoms*, 277:58–69, April 2012. 00009.
- [YS84] Y. Yamamura and Shigeru Shindo. An empirical formula for angular dependence of sputtering yields. *Radiation Effects*, 80(1-2):57–72, January 1984.
- [Zie12] James Ziegler. *SRIM - The Stopping and Range of Ions in Matter*. February 2012.
- [ZLB85] J. F. (James F.) Ziegler, U. Littmark, and J. P. Biersack. *The stopping and range of ions in solids / J.F. Ziegler, J.P. Biersack, U. Littmark*. The Stopping and ranges of ions in matter ; v. 1. Pergamon, New York, 1985. Includes index. Bibliography: p. 308-315.